Optical phonon modes and interband transitions in cubic $Al_xGa_{1-x}N$ films

A. Kasic* and M. Schubert
Universität Leipzig, Fakultät für Physik und Geowissenschaften, Linnéstrasse 5, 04103 Leipzig, Germany

T. Frey, U. Köhler, and D. J. As
Universität Paderborn, Fachbereich Physik, Warburger Strasse 100, 33095 Paderborn, Germany

C. M. Herzinger
J. A. Woollam Co., Inc., 645 M Street, Lincoln, Nebraska 68508
(Received 8 October 2001; published 23 April 2002)

We present a comprehensive study of the phonon mode behavior and the optical interband transitions of cubic $Al_xGa_{1-x}N$ films ($0 \leqslant x \leqslant 0.20$) using spectroscopic ellipsometry from the midinfrared to the vacuum-ultraviolet spectral range (0.05–8.5 eV). The ≈ 0.5-μm-thick $Al_xGa_{1-x}N$ layers were grown by radio-frequency plasma-assisted molecular-beam epitaxy and possess free-electron concentrations in the range of 6×10^{19}–1×10^{20} cm^{-3}. A two-mode behavior for the transverse-optical phonon of $Al_xGa_{1-x}N$ is observed, which is consistent with theoretical predictions. Due to the high free-electron concentration, the observed $Al_xGa_{1-x}N$ fundamental band-gap energy E_0 is subject to a strong Burstein-Moss shift and band-gap renormalization. We quantify the amount of both band-gap shifting mechanisms, and provide an estimate for the composition dependence of the $Al_xGa_{1-x}N$ band-gap energy E_0, which depends approximately linearly on the alloy composition with E_0 (eV) $= 3.19 + 2.77x$ at room temperature and for carrier-depleted material. For cubic GaN, the L-point interband transition E_1 shifts to lower energies with increasing free-electron concentration, whereas the interband transition E_2 remains unshifted. Increasing Al content induces a blueshift (redshift) of the E_1 (E_2) transition of $Al_xGa_{1-x}N$ for $x \leqslant 0.12$. Due to strong broadening effects, both transitions cannot be differentiated anymore for $x \geqslant 0.16$.

DOI: 10.1103/PhysRevB.65.184302 PACS number(s): 63.20.−e, 71.20.Nr

I. INTRODUCTION

Strong stimulated emission from optically pumped cubic GaN/AlGaN double heterostructures in the blue spectral range[1,2] has encouraged further studies of cubic binary and ternary group-III nitrides.[3–13] Compared to the thermodynamically stable hexagonal (α) phase, the metastable cubic (β) phase of the group-III nitrides is expected to possess superior electronic properties: lower carrier scattering resulting in higher carrier mobility, higher doping efficiency, and smaller effective electron masses. Technological advantages for device applications of the cubic modification are the availability of low-cost, large-area, and highly electrically conductive substrates, such as GaAs, and easy cleavage of epilayer and cubic substrate, which is favorable for making laser facets. Furthermore, strong spontaneous polarization fields are avoided in cubic group-III nitride heterostructures. Those polarization fields are present in hexagonal $Al_xGa_{1-x}N$/GaN heterostructures used in light emitting diodes, where the polarization field effects can seriously reduce the optical recombination efficiency. Due to the metastable nature, however, the growth of single-phase cubic nitride films of sufficient homogeneity and crystal quality is still difficult, and in general the crystal quality of cubic epilayers grown so far is inferior to that of the hexagonal nitrides.

Among the cubic group-III nitrides, GaN has been studied most extensively, whereas many fundamental physical properties of ternary cubic group-III nitrides are still unknown. This work is focused on the optical properties of β-$Al_xGa_{1-x}N$, which may serve as cladding layer material for advanced optical devices. So far, most experimental studies of β-$Al_xGa_{1-x}N$ have concentrated on structural properties and the optical characterization of the fundamental band-gap region.[3–13] Our investigations comprise the midinfrared (mid-ir), the near-infrared (near-ir) to ultraviolet (uv), and the vacuum-ultraviolet (vuv) spectral range, where the lattice vibrations, the fundamental band-gap transition E_0, and the interband transitions E_1 and E_2 of β-$Al_xGa_{1-x}N$ occur, respectively.

The vibrational properties of β-$Al_xGa_{1-x}N$ have been investigated theoretically and experimentally by few groups so far. Grille *et al.* studied the lattice dynamics of cubic group-III nitrides using a modified random-element isodisplacement (MREI) approach and a rigid-ion model.[14] For β-$Al_xGa_{1-x}N$ the authors predicted a two-mode behavior for the TO phonon and a one-mode behavior for the LO phonon. Contrary to the results of Grille *et al.*, Liu *et al.* calculated a one-mode behavior for both the TO and LO modes of β-$Al_xGa_{1-x}N$ using the MREI approach as well.[15] Besides the GaN-like TO-phonon mode, Harima *et al.* observed a very weak feature in Raman-scattering spectra of two $Al_xGa_{1-x}N$ films ($x = 0.11$ and 0.75), which the authors attributed to the AlN-like TO-phonon mode.[16] Frey *et al.* reported a single TO-phonon mode using Raman measurements, which were performed on the same sample set investigated in the present work.[3] This mode was assigned to the GaN-like TO phonon, since its frequency revealed a composition dependence very similar to that calculated by Grille *et al.*[14] for the GaN-like TO mode.

So far, three groups have reported the composition dependence of the fundamental band-gap energy E_0 of β-$Al_xGa_{1-x}N$ (direct gap at the Γ point of the Brillouin zone) using spectroscopic ellipsometry (SE). Okumura *et al.* found a linear increase of E_0 vs Al content in the whole composition range.[8] This result was consistent with the linear composition dependence of the highest emission energy $E_{CL}=3.2+1.6x$ observed in cathodoluminescence (CL) spectra of $Al_xGa_{1-x}N$ films, measured at 77 K.[8] Using SE and CL, As *et al.* observed a linear dependence of the band-gap energy on the Al content for $x\leqslant 0.2$.[5] However, Suzuki *et al.* reported a parabolic composition dependence of the $Al_xGa_{1-x}N$ fundamental band-gap energy with a positive bowing parameter of about 1.1 eV for $0\leqslant x\leqslant 1$.[9] Nakadaira and Tanaka found that the photoluminescence (PL) peak energy of a near band-gap emission approximately obeys the relationship $E_{PL}=3.20+1.85x$ for $x\leqslant 0.42$.[13] In good agreement with this result, Wu *et al.* observed that near the band gap emission lines in low-temperature PL spectra of $Al_xGa_{1-x}N$ ($0\leqslant x\leqslant 0.25$) shift approximately linearly to higher energies with increasing Al content.[11] Band-structure calculations of Pugh *et al.* predict a band-gap composition dependence for unstrained $Al_xGa_{1-x}N$ ($x\leqslant 0.57$) without significant band-gap bowing.[17]

The higher-energy interband transitions E_1 and E_2 of β-$Al_xGa_{1-x}N$ ($0<x<1$) have not been investigated so far. In III-V compounds, the band-structure critical point (CP) E_1 is associated with transitions near the L point and/or along the $\langle 111\rangle$ direction.[18] The origin of the CP structure E_2 is more complex and has been attributed to more than one region of the Brillouin zone.[19] For β-GaN, Logothetidis *et al.* assumed that the E_2 CP corresponds mainly to excitations near the X point of the Brillouin zone.[18]

SE in the mid-ir spectral range has recently proven to be a powerful tool for the investigation of lattice vibrations and free-carrier properties of hexagonal thin-film group-III nitride heterostructures and of cubic group-III phosphide and arsenide thin films.[20–24] For near-ir to vuv wavelengths, SE has been employed to study interband transitions and to determine dielectric function spectra of several binary and ternary group-III nitride compounds.[18,25–27] In the present work we use SE from the mid-ir to the vuv spectral range in order to investigate the optical properties of ≈ 0.5-μm-thick β-$Al_xGa_{1-x}N$ films for $0\leqslant x\leqslant 0.20$. Numerically inverted mid-ir SE data provide the TO-phonon mode behavior of β-$Al_xGa_{1-x}N$. The free-carrier concentrations in the β-$Al_xGa_{1-x}N$ films are estimated from the frequencies of the plasmonlike modes. Based on a parametric-model analysis from the near-ir to the uv spectral range, the dependence of the β-$Al_xGa_{1-x}N$ fundamental band-gap energy on the Al content is determined upon correction for Burstein-Moss shift and band-gap renormalization. Finally, we detect the interband transitions E_1 and E_2 of β-$Al_xGa_{1-x}N$ for $x\leqslant 0.12$ in the vuv spectral range.

II. EXPERIMENT

Four unintentionally doped β-$Al_xGa_{1-x}N$ films with $x=0.07$, 0.12, 0.16, and 0.20 (samples A–D) were grown on (001) GaAs substrate at 835 °C by molecular-beam epitaxy using a radio-frequency plasma nitrogen source.[28] The growth rate of the $Al_xGa_{1-x}N$ films was ≈ 80 nm/h, resulting in a film thickness d between 450 and 480 nm. Prior to the growth of the $Al_xGa_{1-x}N$ films, (290–380)-nm-thick β-GaN buffer layers were deposited at 720 °C in order to improve the crystalline quality of the $Al_xGa_{1-x}N$ epilayers. The Al contents determined by Rutherford backscattering spectroscopy are consistent with those obtained from high-resolution x-ray diffraction (HRXRD) measurements. The cubic nature and the crystalline quality of the films were identified by HRXRD experiments. Reciprocal space maps show the comparatively good structural layer quality of the fully relaxed $Al_xGa_{1-x}N$ films.[3] Further details concerning these characterizations and the growth procedure were reported in Refs. 3 and 28 and references therein. The free-electron concentration N_e in the $Al_xGa_{1-x}N$ layers are estimated to be in the range between 6×10^{19} and $1\times 10^{20}\text{cm}^{-3}$ by means of mid-ir SE (see Sec. IV A). High residual oxygen contents, which were detected by secondary ion mass spectroscopy measurements of an $Al_xGa_{1-x}N$/GaN multi-quantum-well structure grown under conditions similar to those of the $Al_xGa_{1-x}N$ samples studied here, may account for these high free-electron concentration values. For comparison, four (0.66–1.05)-μm-thick Si-doped β-GaN films (R_1–R_4), directly grown on the GaAs substrate, are included in our studies as well. These films possess free-electron concentrations from $N_e\leqslant 1\times 10^{17}\text{cm}^{-3}$ (R_1) up to $\approx 6\times 10^{19}\text{cm}^{-3}$ (R_4), which were determined by Hall-effect measurements. A summary of relevant sample details is given in Table I.

All samples were measured at room temperature by variable angle-of-incidence SE for photon energies from ≈ 0.05 to 8.5 eV. The SE spectra in the mid-ir range were taken between 400 and 6000 cm^{-1} (~ 0.05–0.75 eV) with a spectral resolution of 2 cm^{-1}, and at 50° and 70° angles of incidence Φ using a rotating-polarizer, rotating-compensator, Fourier-transform based ellipsometer. A 25-W globar was used as the light source. Details of the mid-ir ellipsometer used here are described in Ref. 29. For the spectral region from 0.75 to 5.5 eV, i.e., from the near-ir to the uv range, a rotating-analyzer ellipsometer equipped with a 75-W Xe lamp as the light source was employed. Measurements were taken at $\Phi=60°$ and 70° with a spectral resolution of 0.01 eV. The near-ir-uv ellipsometer system was equipped with an automated compensator, which allows accurate determination of the ellipsometric parameter Δ. SE measurements in the vuv spectral range (5.5–8.5 eV, wavelengths 225–146 nm) were carried out using a rotating-analyzer ellipsometer with an automated compensator and a dry nitrogen purged sample chamber. The spectra were recorded at $\Phi=60°$ and 70° with a spectral resolution of 0.02 eV. A deuterium lamp was used as the light source.

III. THEORY

A. Spectroscopic ellipsometry

Using SE, the complex dielectric functions of thin-film materials and film thicknesses in a multilayered sample can

TABLE I. TO-phonon mode parameters for cubic GaN and $Al_xGa_{1-x}N$ films, derived from the analysis of mid-ir ellipsometry data. The numerical uncertainties correspond to 90% reliability and are given in parentheses. The alloy composition values were obtained from Rutherford backscattering (RBS) and high-resolution x-ray diffraction (HRXRD) measurements. The film thickness d and the free-electron concentration N_e values result from the near-ir-uv and the mid-ir SE data analysis, respectively.

Sample	x RBS, HRXRD	$d(\mu\text{m})$ SE	N_e $(\text{cm})^{-3}$ Hall or SE[a]	$\omega(\text{TO}^{\text{GaN}})(\text{cm})^{-1}$ SE	Raman[b]	$\gamma(\text{TO}^{\text{GaN}})(\text{cm})^{-1}$ SE	$\omega(\text{TO}^{\text{AlN}})(\text{cm})^{-1}$ SE	$\gamma(\text{TO}^{\text{AlN}})(\text{cm})^{-1}$ SE
R_1	0.00	0.67	$\leqslant 1\times10^{17}$	553.0 (0.2)	555	5.7 (0.5)		
R_2	0.00	0.98	1.4×10^{18}	553.4 (0.2)		7.5 (0.4)		
R_3	0.00	1.05	5.1×10^{19}	552.3 (0.3)		9.6 (1.0)		
R_4	0.00	0.88	6.2×10^{19}	553.1 (0.3)		8.9 (0.7)		
A	0.07	0.46	7×10^{19}	554.3 (0.1)	557	14.4 (0.6)	647.4 (0.4)	13.6 (1.5)
B	0.12	0.48	1×10^{20}	561.2 (0.1)	562	16.2 (0.5)	648.7 (0.6)	16.6 (3.2)
C	0.16	0.47	9×10^{19}	563.8 (0.1)	565	17.9 (0.4)	650.9 (0.5)	17.3 (2.3)
D	0.20	0.46	7×10^{19}	567.3 (0.1)	567	19.7 (0.4)	653.6 (0.5)	15.1 (2.2)

[a]R_1–R_4, Hall; A–D, SE; $m^*=0.15m_0$ was assumed for the SE data analysis.
[b]Reference 3.

be determined. The standard ellipsometric parameters Ψ and Δ are related to the complex reflectance ratio ρ,[30]

$$\rho \equiv \frac{R_p}{R_s} = \tan\Psi \exp(i\Delta), \tag{1}$$

where R_p and R_s are the electric-field reflection coefficients for light polarized parallel (p) and perpendicular (s) to the plane of incidence, respectively. A common representation of the ellipsometric parameters Ψ and Δ is the pseudodielectric function $\langle\varepsilon\rangle$ given by

$$\langle\varepsilon\rangle = \langle\varepsilon_1\rangle + i\langle\varepsilon_2\rangle = \sin^2\Phi\left[1+\left(\frac{1-\rho}{1+\rho}\right)^2\tan^2\Phi\right]. \tag{2}$$

Only in the case of an air ambient over a bare semi-infinite substrate with a perfectly smooth and uncovered surface, the measured pseudodielectric and the intrinsic substrate dielectric function are identical. For layered samples, the SE data need to be analyzed using appropriate layer models.

B. SE data analysis

In order to extract the dielectric function of the layer material of interest from the measured SE data, first a model has to be established, which consists of a sequence of parallel layers with perfectly abrupt interfaces and spatially homogeneous dielectric functions, bound between a semi-infinite substrate and the ambient. Then, a regression analysis (Levenberg-Marquardt fitting algorithm) is performed, where model parameters are varied until calculated and experimental data match as closely as possible. A direct way of obtaining the material's dielectric function of interest (in our case that of $Al_xGa_{1-x}N$) is to numerically invert the experimental SE data for each wavelength and independently of all other spectral data points (point-by-point fit). This procedure requires in our case the knowledge of the $Al_xGa_{1-x}N$ and GaN layer thicknesses as well as the dielectric function of GaN and that of the GaAs substrate. The dielectric function obtained from the point-by-point fit needs to be further compared to line-shape models in order to obtain physically relevant parameters such as phonon mode frequencies. The number of unknown parameters in the regression analysis can be reduced considerably if appropriate parametric-model line-shape functions are used to describe the dielectric function for the layer material of interest. Thereby, all measured spectral data points are simultaneously involved in the regression analysis. In the case of a parametric-model analysis, the measured data are directly connected to the physical parameters of interest and, in principle, the layer thicknesses can also be obtained independently. Furthermore, parametric models prevent wavelength-by-wavelength measurement noise from becoming part of the extracted dielectric function, a possible error source for point-by-point fitted spectra. Further details of the SE data analyses performed here are described in Refs. 20, 31, and 32.

A three-layer model was employed for the SE data analysis of our $Al_xGa_{1-x}N$ samples from the near-ir (1–5 eV) to the vuv (6–8.5 eV) spectral range. This model consists of air/surface-roughness layer/$Al_xGa_{1-x}N$ film/GaN buffer layer/GaAs substrate. The surface-roughness effects were considered by a top layer with optical constants, which were calculated using a linear effective-medium approximation. Here, we assumed a linear average of 50% void and 50% $Al_xGa_{1-x}N$ to simulate the effective optical constants of the surface-roughness layer. For the mid-ir spectral range, surface-roughness effects are negligible due to the large probing wavelengths, and thus a two-layer model is sufficient for the mid-ir SE data analysis. Prior to the analysis of the $Al_xGa_{1-x}N$ layers, the GaAs dielectric function was determined by SE from the mid-ir to the vuv spectral range using several reference samples.

C. Model dielectric function

1. midinfrared range

The contribution of s ir-active polar lattice phonon bands to the dielectric response of semiconductor materials, $\varepsilon^{(L)}(\omega)$, can be described by a factorized form with Lorentzian broadening,[33]

$$\varepsilon^{(\mathrm{L})}(\omega)=\varepsilon_\infty\prod_{k=1}^{s}\frac{\omega_{\mathrm{LO},k}^2-\omega^2-i\omega\gamma_{\mathrm{LO},k}}{\omega_{\mathrm{TO},k}^2-\omega^2-i\omega\gamma_{\mathrm{TO},k}}. \tag{3}$$

The parameters $\omega_{\mathrm{TO},k}$, $\gamma_{\mathrm{TO},k}$, $\omega_{\mathrm{LO},k}$, and $\gamma_{\mathrm{LO},k}$ denote the frequencies and damping values of the kth TO- and LO-phonon modes, respectively, and ε_∞ is the high-frequency dielectric constant. The free-carrier contribution to the material's dielectric function, $\varepsilon^{(\mathrm{FC})}(\omega)$, is commonly written in the classical Drude approximation as

$$\varepsilon^{(\mathrm{FC})}(\omega)=-\varepsilon_\infty\frac{\omega_p^2}{\omega(\omega+i\gamma_p)}. \tag{4}$$

The screened plasmon frequency ω_p and plasmon damping γ_p are related to the concentration N, the effective mass m^*, and the mobility μ of the free carriers by the following equations:[34]

$$\omega_p=\sqrt{\frac{Ne^2}{m^*\varepsilon_0\varepsilon_\infty}} \tag{5}$$

and

$$\gamma_p=\frac{e}{m^*\mu}, \tag{6}$$

where e is the electrical unity charge and ε_0 is the vacuum permittivity.

Mid-ir SE data possess high sensitivity to TO-phonon mode parameters of thin films, because the TO vibrations are excited resonantly by the ir probe beam resulting in distinct mid-ir SE spectral features. The TO-phonon mode frequencies can be well obtained from the spectral positions of the maxima of $\mathrm{Im}\{\varepsilon(\omega)\}$ with $\varepsilon(\omega)=\varepsilon^{(\mathrm{L})}(\omega)+\varepsilon^{(\mathrm{FC})}(\omega)$, even in the case of strong phonon and plasmon damping. Sensitivity to longitudinal phonon mode frequencies of individual layers in complex heterostructures is provided by the well-known Berreman-polariton effect in thin polar dielectric films.[35] The ir radiation excites surface polaritons of transversal magnetic character at the boundary of two media whose dielectric functions fulfill certain conditions.[36,37] The incident wave is guided along the thin-film interfaces near wave numbers where the index of refraction approaches unity. In this spectral region, the ellipsometry data have high sensitivity to the longitudinal phonon frequency and damping parameters.

The consideration of two TO-LO-phonon bands [Eq. (3)] for the parametrization of the β-$Al_xGa_{1-x}N$ dielectric function has proven to be insufficient to model the experimental SE data of our $Al_xGa_{1-x}N$ samples in the mid-ir (400–6000 cm^{-1}) spectral range. Increasing the number k of TO-LO-phonon bands, however, has made phonon mode assignment very difficult. Therefore, the experimental mid-ir SE data were numerically inverted using the wavelength-by-wavelength approach. The thickness values of the $Al_xGa_{1-x}N$ epilayer and GaN buffer layer, which are prerequisites for the point-by-point data inversion procedure, were taken from the parametric data analysis in the near-ir-uv spectral range (see below). Local line-shape analyses using Lorentzian oscillators were then employed to simulate the wavelength-by-wavelength inverted data, i.e., the $Al_xGa_{1-x}N$ mid-ir dielectric function spectra, thus providing the TO and plasmon mode parameter values for the $Al_xGa_{1-x}N$ films. Details of the point-by-point fit procedure for ir ellipsometry data analysis were also discussed recently in Ref. 23 and references therein.

2. Near-infrared–ultraviolet range

In the near-ir-uv (1.0–5.0 eV) as well as in the vuv (6.0–8.5 eV) spectral range, the $Al_xGa_{1-x}N$ (GaN) dielectric function was parametrized using a modified CP model dielectric function (MDF) approach.[38,39] Within this MDF approach the contribution of each CP (C) to the material's dielectric function is described by line-shape functions, which depend on the photon energy $E=\hbar\omega$,

$$C_j(A_j,E_j,\Gamma_j,\phi_j,\mu_j)\equiv A_j\exp(i\phi_j)(E_j-E-i\Gamma_j)^{-\mu_j}. \tag{7}$$

The parameters E_j, Γ_j, and A_j denote the transition energy, the Lorentzian broadening, and the magnitude of the CP structure within the dielectric function spectrum, respectively. The phase angle ϕ_j is related to the amount of mixture of two adjacent CP's. Within the standard CP model, the exponent μ_j is related to the dimension δ of the van Hove singularity corresponding to the CP: $\mu_j=1-\delta/2$. Here, we employed a modification of the CP model approach, where μ_j is treated as an adjustable parameter.[40]

For the near-ir-uv spectral range, the $Al_xGa_{1-x}N$ (GaN) dielectric function was parametrized by

$$\varepsilon(\omega)=c+C_0+A_p/(E_p^2-E^2). \tag{8}$$

The pole [third term in Eq. (8)] allows for contributions of higher-energy CP's to the material's dielectric function from spectral regions outside the range investigated here. The best-fit values for the phase angle were $\phi_0\approx\pi$ for all samples studied. Using Eq. (8) for the parametrization of the $Al_xGa_{1-x}N$ dielectric function in the near-ir-uv spectral range, the $Al_xGa_{1-x}N$ fundamental band-gap energy E_0 and the thicknesses of all sample layers were determined. The thickness of the surface-roughness layer obtained from the SE data analysis in the near-ir-uv spectral range was between 4 and 7 nm for all $Al_xGa_{1-x}N$ samples and was kept constant during the SE data analysis in the vuv spectral range.

3. Vacuum-ultraviolet range

For the parametrization of the $Al_xGa_{1-x}N$ (GaN) dielectric function in the vuv spectral range, a sum of two CP expressions was employed for $x\leqslant 0.12$ (see Sec. IV C) to describe contributions from the CP structures E_1 and E_2 occurring within this spectral range:[38]

$$\varepsilon(E)=c+\sum_{j=1,2}C_j. \tag{9}$$

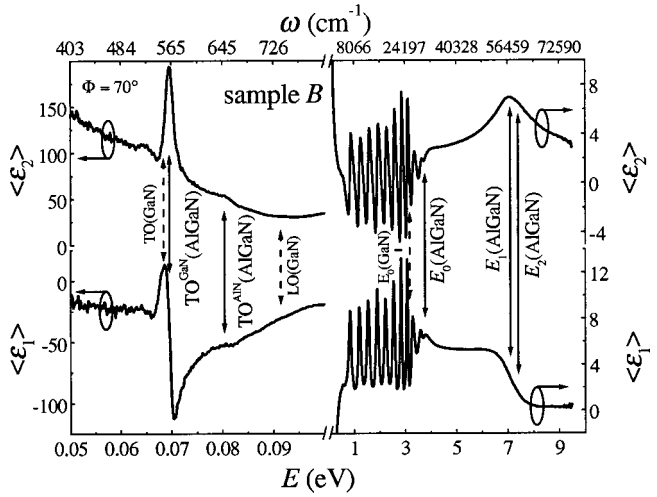

FIG. 1. Real and imaginary parts of the pseudodielectric function of sample *B*, measured from the mid-ir to the vuv spectral range. The observed phonon mode and interband transition energies are marked by vertical arrows, together with the assignment according to the SE data analyses. Solid and dashed arrows refer to the $Al_{0.12}Ga_{0.88}N$ layer and the GaN buffer layer, respectively. Note the different scales on the left and right axes.

In the regression analysis, we assumed $\mu_2=1$, i.e., the E_2 CP was assumed to be excitonic, which considerably reduces correlations among the parameters of both CP's. The exponent μ_1 of the E_1 CP term was allowed to vary during the regression analysis, and the best-fit values for this parameter were obtained as ≈ 0.4 for all $Al_xGa_{1-x}N$ ($x \leqslant 0.12$) and GaN films. For $x \geqslant 0.16$, a single CP contribution was used to model the experimental SE data (see Sec. IV C).

IV. RESULTS AND DISCUSSION

Figure 1 presents experimental ellipsometry data of sample *B* in terms of the pseudodielectric function, which are typical for all $Al_xGa_{1-x}N$/GaN heterostructures studied here. In the mid-ir, the spectra are dominated by features originating from lattice vibrations of the heterostructure components AlGaN and GaN. In the transparency region of the heterostructure, i.e., between the reststrahlen bands and the fundamental band gaps of the sample layer materials, pronounced Fabry-Perot interference oscillations occur due to multiple internal reflections within the heterostructure. Between about 7.0 and 7.5 eV, $\langle \varepsilon_2 \rangle$ reveals an asymmetric double structure, which originates from the optical interband transitions E_1 and E_2 of $Al_xGa_{1-x}N$.

A. Phonon modes and free-carrier properties

Figure 2(a) shows measured mid-ir $\langle \varepsilon_1 \rangle$ and $\langle \varepsilon_2 \rangle$ spectra of sample *D*. For comparison, in Fig. 2(b) the $\langle \varepsilon \rangle$ spectra of the reference sample R_1 are depicted, whose GaN film possesses optical properties similar to the GaN buffer layers in the $Al_xGa_{1-x}N$ samples *A*–*D*. In the mid-ir spectral range the material's dielectric functions of all $Al_xGa_{1-x}N$ and GaN films were obtained from wavelength-by-wavelength numerical inversion of the measured $\langle \varepsilon \rangle$ spectra. The ε_2 spectra of all $Al_xGa_{1-x}N$ films reveal a two-mode behavior for the $Al_xGa_{1-x}N$ TO-phonon for $x \leqslant 0.20$, The GaN-like TO mode (TO^{GaN}) appears as a distinct peak and the AlN-like TO mode (TO^{AlN}) appears as a weak, but well-resolved shoulder. In Fig. 3, the ε_2 spectra of all $Al_xGa_{1-x}N$ films are displayed in the range of both $Al_xGa_{1-x}N$ TO-phonon modes. In order to determine the TO mode frequencies and damping values, the $Al_xGa_{1-x}N$ and GaN ε_2 spectra were locally described by Lorentzian line shapes (solid lines in Fig. 3). The TO-phonon mode parameters of all $Al_xGa_{1-x}N$ and GaN films derived from the Lorentzian line-shape best-fit calculations are listed in Table I. In Fig. 2, the two TO-phonon mode positions of the $Al_{0.20}Ga_{0.80}N$ epilayer (sample *D*) and the TO and LO frequencies of the GaN buffer layer are marked by vertical arrows. In the ε_2 spectrum of the GaN sample R_1, a weak shoulder (asterisk in Fig. 3) occurs at the

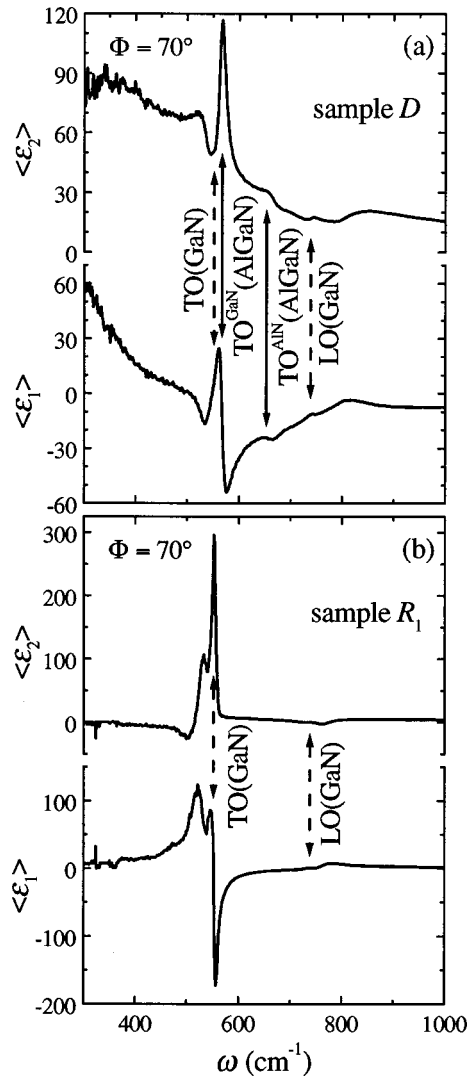

FIG. 2. Pseudodielectric function spectra of samples *D* (a) and R_1 (b), measured in the mid-ir spectral range. The spectral positions of the optical-phonon modes of GaN and $Al_{0.20}Ga_{0.80}N$ are marked by dashed and solid arrows, respectively. The noise in the lower part of the spectra is mainly due to decreasing intensity of the ir light source for small wave numbers.

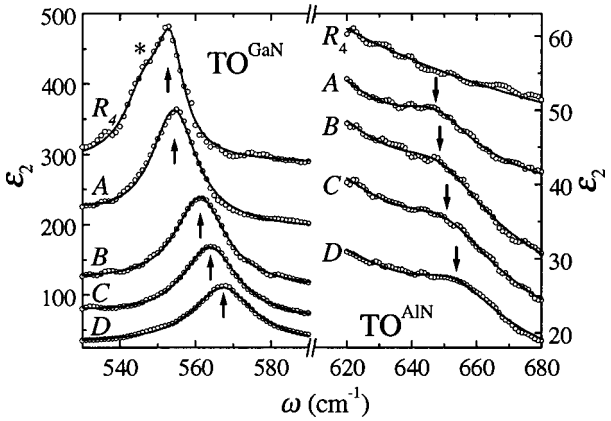

FIG. 3. Imaginary parts of the $Al_xGa_{1-x}N$ (GaN) dielectric functions for samples $A-D$ and R_4 near the GaN-like and AlN-like TO-phonon mode. Symbols, wavelength-by-wavelength inverted data; lines, best-fit spectra using local Lorentzian line shapes. The phonon-mode positions resulting from the best-fit calculations are marked by arrows. For convenience, the spectra of samples R_4, A, B, and C on the left (right) side are shifted vertically by 260, 160, 50, and 10 (38, 18, -5, and -8), respectively.

low-frequency side of the GaN TO-phonon mode peak. Similar features centered at about 545 cm^{-1} are present in the ε_2 spectra of the GaN samples R_2-R_4 as well (not shown in Fig. 3). As the origin, we suggest a disorder-induced lattice vibration due to the Si doping of the GaN films, but no clear assignment of the observed feature can be given yet.

The composition dependences of both $Al_xGa_{1-x}N$ TO-phonon mode frequencies are shown in Fig. 4 together with

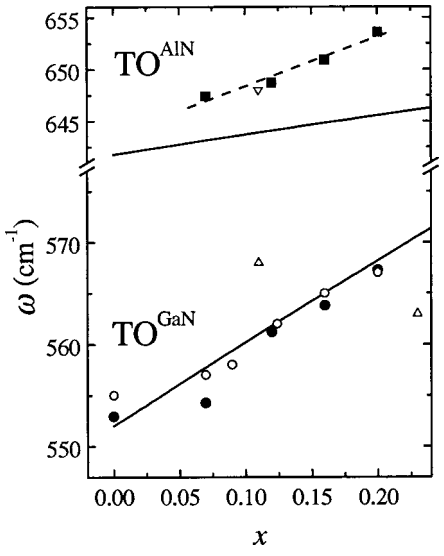

FIG. 4. Composition dependences of the GaN-like and AlN-like TO-phonon frequencies, determined by the mid-ir SE data analysis (full symbols). For comparison, the GaN-like TO mode frequencies obtained from Raman-scattering measurements on the same sample set are included (open circles, Ref. 3). Open triangles: Raman data from Ref. 16. Solid lines: calculated $Al_xGa_{1-x}N$ TO-phonon mode behavior, Ref. 14. The observed approximately linear composition dependence of the AlN-like TO phonon frequency (dashed line) shows a stronger increase vs x than theoretically predicted.

theoretical predictions of Grille *et al.*[14] and Raman-scattering results reported in Refs. 3 and 16. For the GaN-like TO mode, the phonon frequencies determined by SE are consistent with both the Raman-scattering results obtained for the same sample set[3] and the theoretical mode behavior calculated in Ref. 14. For the AlN-like TO mode, however, the approximate linear dependence of the phonon frequency on the Al content (dashed line in Fig. 4) shows a stronger increase vs x than theoretically predicted.[14] In μ-Raman spectra taken from the same sample set and depicted in Ref. 3, the AlN-like TO mode is submerged by a broadband, which is characteristic for highly damped plasmon excitations in the frequency region between the TO and LO mode as shown, e.g., for N-type cubic GaN by Ramsteiner *et al.*[41] Thus, the AlN-like TO mode was not detected in Ref. 3. The primary measurement quantity of infrared ellipsometry is the dielectric function from which the infrared-active mode parameters can be obtained most directly upon its line-shape analysis. Phonon modes of small polarity, potentially inaccessible by Raman-scattering techniques, can still be retrieved from ε with high accuracy.

Free-carrier plasmons interact with long-wavelength LO phonons via the electric fields associated with both types of elementary excitations. Hall-effect measurements in van der Pauw geometry[3] revealed that all $Al_xGa_{1-x}N$ films possess degenerated free-electron gases with concentrations of $\approx 10^{20}$ cm^{-3} and mobilities of about 20 $cm^2/V\,s$. For such small free-carrier mobility values, $\gamma_p \approx \omega_p$ and the plasmon excitations are highly damped. As demonstrated by Giehler and Jahne[42] for CdS and GaP ($s=1$), the upper of the two coupled LO-phonon-plasmon mode branches (LPP^+) then becomes plasmonlike for $\omega_p \gg \omega_{LO}$, and the lower branch (LPP^-) represents a LO phonon screened by free carriers, whose frequency approaches asymptotically the TO-phonon mode frequency. Because for GaN-rich β-$Al_xGa_{1-x}N$ a strong GaN-like TO-LO phonon band dominates the mid-ir dielectric function,[43] the situation should be similar to that of CdS and GaP. Figure 5 shows the spectral region, where the high-energy plasmonlike mode branch appears as a strongly broadened maximum of $\mathrm{Im}(-1/\varepsilon)$, which is localized between 2500 and 3100 cm^{-1} for all $Al_xGa_{1-x}N$ layers. For the following estimate of the free-carrier concentration in the $Al_xGa_{1-x}N$ layers, we neglect the weak AlN-like TO-LO-phonon band and approximate the mid-ir dielectric function by $\varepsilon(\omega)=\varepsilon^{(L)}(\omega)+\varepsilon^{(FC)}(\omega)$ with $s=1$. Only in the case of weak plasmon damping, the frequencies of the longitudinal modes (LO phonons, plasmons, and LPP modes) correspond to the maxima of $\mathrm{Im}(-1/\varepsilon)$. For high plasmon damping values and $\omega_p \gg \omega_{LO}-\omega_{TO}$, the spectral position of the high-energy maximum of $\mathrm{Im}(-1/\varepsilon)$ is approximately given by $(\omega_p^2-\gamma_p^2/4)^{1/2}$. For our $Al_xGa_{1-x}N$ films with $\omega_p \approx \gamma_p \approx 3000$ cm^{-1}, this yields a redshift of the high-energy maximum of $\mathrm{Im}(-1/\varepsilon)$ with respect to the plasmon frequency of about $0.13\omega_p$. Considering this correction, the free-electron concentrations N_e of the $Al_xGa_{1-x}N$ films were estimated to be in the range between 6×10^{19} and $1\times10^{20} cm^{-3}$. For this approximation we used Eq. (5), set the high-frequency dielectric constant ε_∞ to 5.0, and assumed the effective elec-

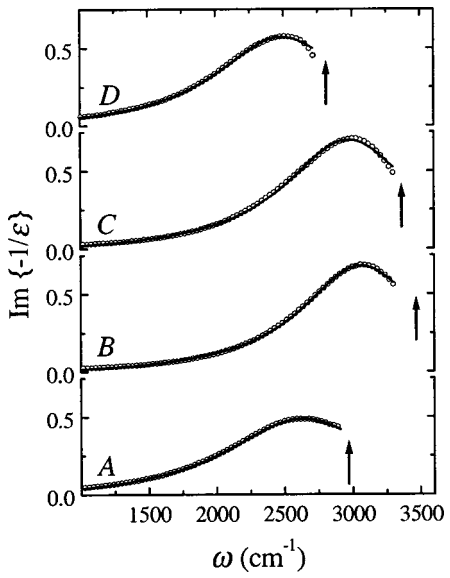

FIG. 5. Im$(-1/\varepsilon)$ for all four $Al_xGa_{1-x}N$ films (samples *A*-*D*) in the spectral range of the plasmonlike mode branch. Symbols, wavelength-by-wavelength inverted data; lines, best-fit spectra using a local Lorentzian line shape. Because the $Al_xGa_{1-x}N$ heterostructures become transparent above the $Al_xGa_{1-x}N$ reststrahlen band, the wavelength-by-wavelength numerical data inversion fails for wave numbers ~ 200 cm^{-1} above the maximum of Im$(-1/\varepsilon)$. The positions of the maxima of Im$(-1/\varepsilon)$ upon correction for plasmon damping effects (arrows) yield the free-electron concentration values of the $Al_xGa_{1-x}N$ films.

tron mass m_e^* to be $0.15m_0$ for all $Al_xGa_{1-x}N$ films, which is the only available experimental value for β-GaN;[44] an average of several calculated m_e^* values is listed in Ref. 45. The N_e values obtained from this approximation are in good agreement with results from Hall-effect measurements performed on the same samples.[3,5]

Carrier-depleted surface layers can be identified at infrared wavelengths upon the Berreman effect, where a guided surface polariton is excited near the LO-phonon frequency of the near-surface sample area. This Berreman polariton causes a subtle feature in the ellipsometric spectra, which can be used to quantify the depletion layer thickness and the uncoupled LO-phonon mode frequency of the layer material. First ir-ellipsometric measurements of thin depletion layers ($\approx$10–20 nm in the Schottky approximation) were performed on high-quality cubic (*n*-type GaAs) (Ref. 24) and hexagonal (*n*-type GaN) (Ref. 46) III-V compounds. However, large TO lattice-resonance broadening causes overdamping of the surface polariton, and its spectral features will then fall within the data noise, as it is likely the case for our $Al_xGa_{1-x}N$ films. Here we do expect a carrier-depleted surface layer due to the high free-carrier concentration, but no appreciable signature in the data around the $Al_xGa_{1-x}N$ LO mode could be observed. Therefore, we treated the $Al_xGa_{1-x}N$ layers to be homogeneous, and their dielectric functions ε were determined through the wavelength-by-wavelength numerical inversion of the SE data. Subtle features, caused by the surface depletion layers, may thereby propagate into ε of the $Al_xGa_{1-x}N$ films, but only in the range of the uncoupled LO-phonon modes. Neglecting the surface depletion layers does not affect the spectral regions of the TO-phonon and plasmonlike mode frequencies, which are of current interest here.

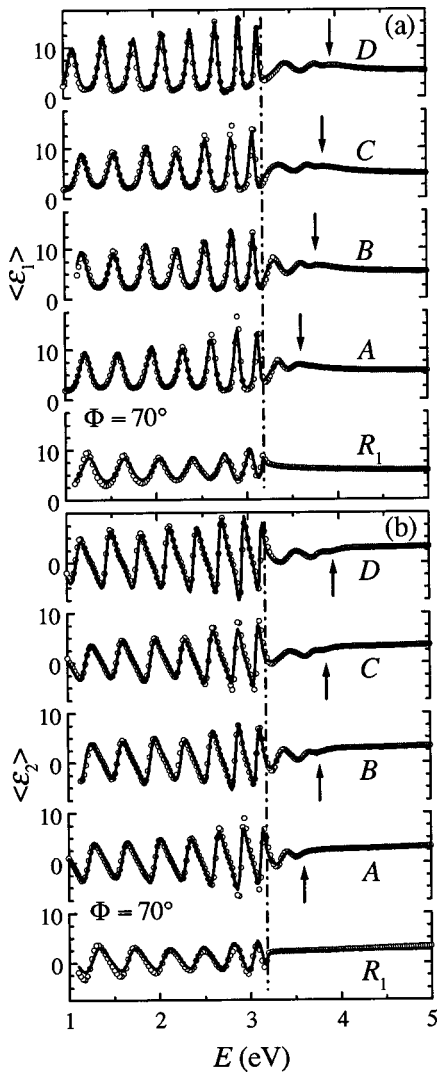

FIG. 6. Real (a) and imaginary parts (b) of the pseudodielectric functions of all $Al_xGa_{1-x}N$ samples (*A*-*D*) and of the GaN sample R_1 from the near-ir to the uv spectral range. The optical properties of the highly resistive GaN film of sample R_1 are similar to those of the GaN buffer layers in samples *A*–*D*. Symbols, experimental data; solid lines, best-fit calculated MDF spectra. The fundamental band-gap energies of $Al_xGa_{1-x}N$ and GaN are marked by arrows and vertical dash-dotted lines, respectively.

B. E_0 transition

In Fig. 6 the measured and best-fit $\langle \varepsilon_1 \rangle$ (a) and $\langle \varepsilon_2 \rangle$ (b) spectra of all $Al_xGa_{1-x}N$ samples are depicted in the near-ir-uv region. For comparison, the spectra of the highly resistive GaN reference sample R_1 are included as well, which possesses free-carrier properties similar to those of the GaN buffer layers in samples *A*–*D*. The best-fit spectra shown in Fig. 6 were calculated using the CP MDF approach as described in Sec. III. Two types of interference oscillations can

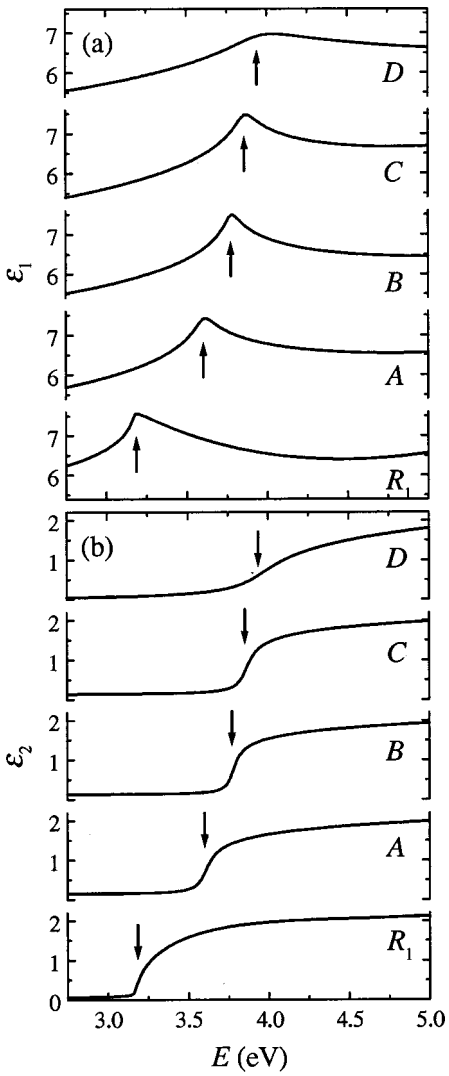

FIG. 7. Real (a) and imaginary parts (b) of the best-fit $Al_xGa_{1-x}N$ (GaN) MDF obtained from the near-ir-uv SE data analysis. The $Al_xGa_{1-x}N$ (GaN) fundamental band-gap energies are marked by arrows.

be observed in the $Al_xGa_{1-x}N$ SE spectra. For photon energies below the GaN band-gap (~ 3.2 eV, marked by vertical dash-dotted lines in Fig. 6), the interference oscillations arise from multiple reflections within the whole epitaxial layer stack. In the spectral range between the E_0 energies of GaN and $Al_xGa_{1-x}N$, the interference oscillations are mostly due to internal reflections within the ternary layer.

In the near-ir-uv spectral range, the complex $Al_xGa_{1-x}N$ dielectric function spectra, the energy E_0 and broadening parameters Γ_0 of the fundamental band-gap transition, and the thickness d of the $Al_xGa_{1-x}N$ epilayers (see Table I) were determined by the SE data analysis. Figure 7 exhibits the real and imaginary parts of the dielectric functions of all $Al_xGa_{1-x}N$ films near the fundamental band gap. With increasing Al content, the band gap clearly shifts to higher energies. For the film with the highest Al content ($x=0.20$) the band-gap structure is considerably broadened ($\Gamma_0 \approx 300$ meV), which may indicate a comparatively lower crystalline quality of this film (see Table II for Γ_0 values). The best-fit values for the band-gap energy parameter E_0 are listed in Table II and plotted vs x in Fig. 8 (full squares). For comparison, the band-gap energy values of the GaN reference films R_1 and R_4, obtained from our SE data analysis, are included in Fig. 8 as well (R_1, closed triangle; R_4, inverted closed triangle). For the highly resistive GaN film R_1 with $N_e \leqslant 1\times10^{17}\text{cm}^{-3}$, E_0 was determined as 3.183 (± 0.003) eV, which is in very good agreement with the GaN band-gap energy values reported by Petalas *et al.*[47] and Köhler *et al.*[48] using SE as well. With increasing free-electron concentration, we observe a strong blueshift of the GaN band gap. For the highly *n*-conductive GaN film with $N_e = 6.2\times10^{19}\text{cm}^{-3}$ (sample R_4), this blueshift is determined as 185 meV with respect to sample R_1. This observation can be well explained by the presence of band filling effects (Burstein-Moss shift, BMS) accompanied by many-body effects. Burstein-Moss shifts of the fundamental band gap have been observed for several group-III nitride materials, e.g., for α-GaN and α-InGaN.[49–51] The amount of such a band-gap blueshift can be roughly estimated for the case of extreme degeneracy by relating the Fermi energy E_F with the free-electron concentration N_e as follows:[52]

$$\Delta E_0^{\text{BMS}} = \frac{\hbar^2}{2m_e^*}(3\pi^2 N_e)^{2/3}. \tag{10}$$

In addition to the BMS, high impurity and high carrier densities lead to the formation of band tails and to correlation effects among the free carriers, respectively, both resulting in a band-gap reduction. These band-gap renormalization (BGR) effects thus act oppositely to the BMS and can be estimated by the following empirical relationship:[50,53]

$$\Delta E_0^{\text{BGR}} = -\alpha N_e^{1/3}. \tag{11}$$

For $m_e^* = 0.15 m_0$,[44] and under the assumption that BMS and BGR effects are negligible for the highly resistive GaN sample R_1, the BGR coefficient α for cubic GaN was obtained as 5.5×10^{-8} eV cm, averaged between those obtained from the highly degenerated GaN films (samples R_3 and R_4). This value is consistent with the BGR coefficient $\alpha = 5.7\times10^{-8}$ eV cm determined by As *et al.* from low-temperature PL spectra of a highly Si-doped cubic GaN film.[54] For hexagonal *n*-type GaN, Yoshikawa *et al.* observed a BGR coefficient of $\alpha = 4.7\times10^{-8}$ eV cm.[55]

The presence of a strong BMS attenuated by many-body effects may further be responsible for the significantly blueshifted band gap of our $Al_xGa_{1-x}N$ films compared to the $Al_xGa_{1-x}N$ band-gap energy values observed by Okumura *et al.*[8] and Suzuki *et al.*[9] using SE (see Fig. 8).[56] Unfortunately, the authors did not mention about the free-carrier concentration in their $Al_xGa_{1-x}N$ epilayers. The effective band-gap blueshift of our $Al_xGa_{1-x}N$ films, originating from BMS [Eq. (10)] and BGR [Eq. (11)], can be tentatively estimated using the BGR coefficient obtained from the analysis of our degenerated GaN samples and assuming $m^* = 0.15 m_0$. The resulting band-gap energy values for samples A–D are included in Table II and depicted in Fig. 8 as closed circles.

TABLE II. Energy and broadening values of the interband transitions E_0 (fundamental band gap), E_1, and E_2 for cubic GaN and $Al_xGa_{1-x}N$ films. The numerical uncertainties correspond to 90% reliability and are given in parentheses.

Sample	x RBS, HRXRD	E_0 (eV) SE	Γ_0 (meV) SE	E_1 (eV) SE	E_2 (eV) SE	Γ_1 (meV) SE	Γ_2 (meV) SE
R_1	0.00	3.183 (0.003)	19 (6)	7.235 (0.007)	7.572 (0.004)	312 (11)	130 (4)
R_2	0.00	3.209 (0.003)	55 (2)	7.106 (0.007)	7.568 (0.007)	241 (14)	179 (6)
R_3	0.00	3.289 (0.011)	125 (13)	7.005 (0.007)	7.556 (0.011)	278 (16)	257 (10)
R_4	0.00	3.368 (0.005)	110 (11)	[a]	[a]	[a]	[a]
A	0.07	3.601 (0.010) 3.403[b]	81 (15)	7.131 (0.007)	7.438 (0.013)	332 (11)	215 (12)
B	0.12	3.773 (0.007) 3.504[b]	62 (9)	7.145 (0.011)	7.398 (0.024)	334 (26)	407 (11)
C	0.16	3.857 (0.010) 3.603 [b]	89 (15)	7.042 [c] (0.003)		268 [c] (7)	
D	0.20	3.938 (0.021) 3.762[b]	293 (28)	7.080 [c] (0.006)		347 [c] (7)	

[a]No data available.

[b]Upon correction for BMS and BGR (see text).

[c]E_1 and E_2 transitions cannot be differentiated.

Including the band-gap value measured for the highly resistive GaN film R_1, the alloy composition of the $Al_xGa_{1-x}N$ band-gap energy upon correction for BMS and BGR obeys approximately the linear dependence $E_0(x)=a_0+a_1x$ with $a_0=3.19(\pm0.02)$ eV and $a_1=2.77(\pm0.16)$ eV for $0\leqslant x\leqslant0.20$. This band-gap energy dependence on the alloy composition is displayed by the solid line in Fig. 8. Pugh *et al.* employed a semiempirical pseudopotential method in order to calculate the composition dependence of the band-gap energy for unstrained β-AlGaN and observed no significant band-gap bowing.[17] These band-structure calculations further predict a direct-indirect crossover at $x=0.57$, which is shown in Fig. 8 by the composition dependences of the band gaps at the Γ and X points of the Brillouin zone (dashed lines). As can be seen from Fig. 8, for $x\leqslant0.20$, the linear $E_0(x)$ relationship found by our SE data analysis taking into account the BMS and BGR corrections agrees excellently with the composition dependence of the band gap at the Γ point, calculated by Pugh *et al.*[17] The linear coefficient a_1 obtained for our $Al_xGa_{1-x}N$ films, however, is significantly larger than those observed by Okumura *et al.*[8] ($a_1=1.6$ eV for $0\leqslant x\leqslant1$) and Nakadaira and Tanaka[13] ($a_1=1.85$ eV for $0\leqslant x\leqslant0.23$) for near band-gap CL and PL emissions, respectively. Suzuki *et al.*[9] reported a small positive bowing parameter (1.1 eV) for the $Al_xGa_{1-x}N$ band gap in the whole composition range. For α-AlGaN, the band-gap energy values reported so far vary widely. Upon a detailed analysis of the existing data considering the influence of different growth conditions, Lee *et al.*[57] recommended the intrinsic band gap bowing parameter for unstrained α-AlGaN to be 0.62 (±0.45) eV.

C. E_1 and E_2 transitions

So far, neither experimental nor theoretical investigations of the β-$Al_xGa_{1-x}N$ optical response for $0<x<1$ in the vuv spectral range have been performed. In Fig. 9, we present the measured pseudodielectric function spectra (symbols) of all $Al_xGa_{1-x}N$ samples in the vuv spectral range. The best-fit $\langle\varepsilon\rangle$ spectra (solid lines) were calculated using the CP MDF for $Al_xGa_{1-x}N$ and GaN, as described in Sec. III. For comparison, the $\langle\varepsilon\rangle$ spectra of the GaN reference samples R_1–R_3 are included in Fig. 9 as well. Due to the small penetration depth of the vuv probe beam in this spectral region, the measured pseudodielectric function and the dielectric function of the top layer material are nearly equivalent, ex-

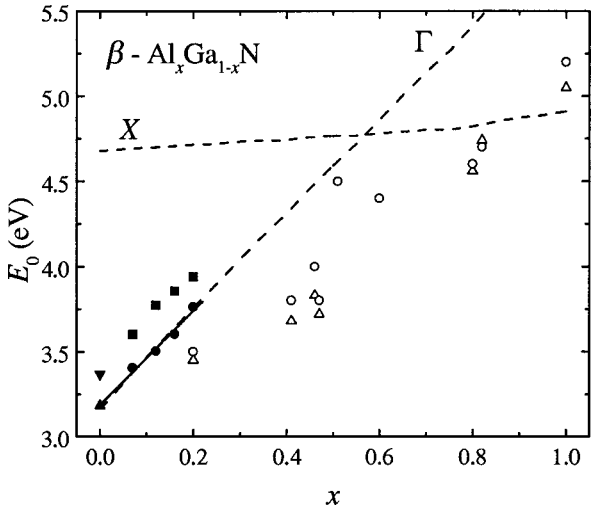

FIG. 8. Composition dependence of the fundamental band-gap energy E_0 at room temperature, determined by several authors using SE. Full symbols, this work (squares, as measured; circles, corrected for BMS and BGN; triangle, sample R_1 as measured; inverted triangle, sample R_4, as measured); open circles, Ref. 8; open triangles, Ref. 9. The dashed lines show results from semiempirical pseudopotential calculations for the $Al_xGa_{1-x}N$ band gaps at the Γ and X points of the Brillouin zone, Ref. 17.

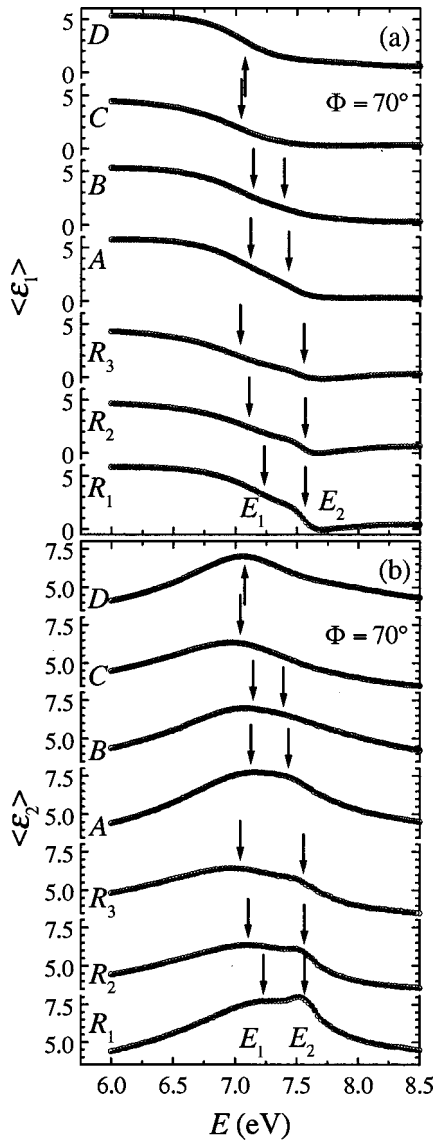

FIG. 9. Real (a) and imaginary parts (b) of the pseudodielectric functions of all $Al_xGa_{1-x}N$ films (*A*-*D*) and of the GaN samples R_1–R_3 in the vuv spectral range. Symbols, experimental data; solid lines, best-fit calculated MDF spectra. The $Al_xGa_{1-x}N$ (GaN) interband transitions E_1 and E_2 are marked by arrows. For $x \geqslant 0.16$, the E_1 and E_2 transitions cannot be differentiated anymore.

cept for contributions from surface contaminants, roughness, and native oxides.[58]

The vuv $\langle \varepsilon_2 \rangle$ spectrum of the highly resistive GaN sample R_1 shows an asymmetric double structure, which consists of a shoulderlike feature at ~7.2 eV and a maximum at ~7.6 eV (both marked by arrows). Logothetidis *et al.*[18] derived vuv ε_2 spectra of β-GaN using SE and observed a spectral structure peaking at ~7.0 and ~7.6 eV, which is quite similar to the double structure found in the $\langle \varepsilon_2 \rangle$ spectra of our β-GaN reference films. The authors attributed this double-peak structure to the optical interband transitions E_1 and E_2 of β-GaN by comparing the energetic positions of both transitions with band-structure calculations. We follow this assignment and identify the double structure

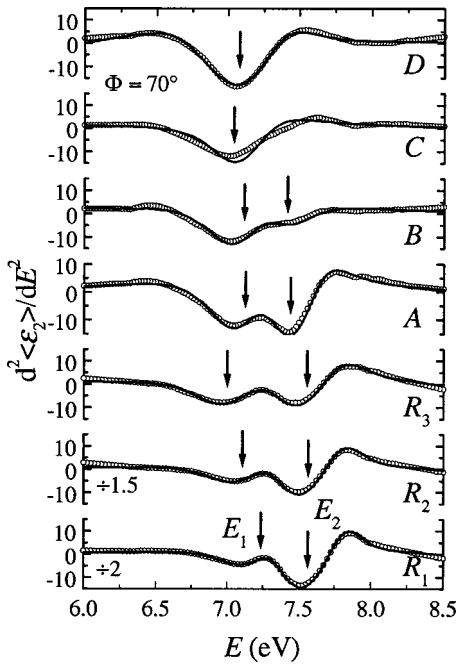

FIG. 10. Second derivates of the $\langle \varepsilon_2 \rangle$ spectra depicted in Fig. 9(b). Symbols, experimental data; solid lines, best-fit calculated MDF spectra. Both interband transitions are marked by arrows. For $x \geqslant 0.16$, the E_1 and E_2 transitions cannot be differentiated anymore.

observed in the $\langle \varepsilon_2 \rangle$ spectra of the samples *A* and *B* as features caused by the AlGaN interband transitions E_1 and E_2.

Figure 10 shows the second derivatives of the measured (symbols) and best-fit (solid lines) $\langle \varepsilon_2 \rangle$ spectra, which are depicted in Fig. 9(b). The derivatives were calculated by locally fitting a third-order polynomial to the $\langle \varepsilon_2 \rangle$ spectra using 25 data points centered around the spectral point of interest. For all GaN films and $Al_xGa_{1-x}N$ samples *A* and *B*, the E_1 and E_2 CP features can be clearly resolved. The best-fit calculations for these samples were performed using one CP expression for each of the two interband transitions as given by Eq. (9); the best-fit values for the transition energy and broadening parameters are listed in Table II. For $x \geqslant 0.16$ (samples *C* and *D*), the E_1 and E_2 CP features are considerably broadened, and a single spectral feature occurs only. Therefore, a single CP contribution to the MDF is sufficient to model the experimental data of these $Al_xGa_{1-x}N$ films in the vuv spectral range.

First, we concentrate on the interband transitions of β-GaN. For the samples R_1–R_3, the E_1 transition energy of GaN is in the range between 7.24 and 7.01 eV and reveals a strong dependence on the free-carrier concentration of the film. The increase of the free-electron concentration from $N_e \leqslant 1\times10^{17}\text{cm}^{-3}$ (R_1) to $N_e = 5.1\times10^{19}\text{cm}^{-3}$ (R_3) leads to a redshift of the E_1 CP energy of 0.23 eV. Our results for the GaN E_1 CP energy are consistent with *ab initio* calculations of the long-wavelength dielectric function of β-GaN, which included the electron-hole interaction and provided a distinct peak in ε_2 at 6.8 eV,[59] and with SE data from Janowitz *et al.*, which show a peak in ε_2 at ≈ 7 eV.[60]. Furthermore, Logothetidis *et al.*[18] determined the E_1 CP energy at RT as

6.93 (± 0.13) eV for β-GaN, but did not give information on the free-carrier concentration of their film. For wurtzite material, the E_1 interband transition was reported to be between 6.9 and 7.0 eV, i.e., in the same energy range as for β-GaN.[18,59,61–63] According to the work by Kuball *et al.*,[64] who studied the doping dependence of the E_1 CP energy in *n*- and *p*-type GaAs, a carrier-depleted surface layer influences the CP energy for samples with intermediate free-carrier concentration values N, such as here for sample R_2 (for large N the depletion layer is too small, and for small N the optical effects are negligible). Second-order perturbation-theory calculations within the parabolic band model, which included free-carrier screening of substitutional impurity potentials in bulk material, lead to the dependence of the relative CP energy shift on N : $\Delta E \propto N^{1/2}$.[65] A carrier-depleted surface layer causes unscreening of impurities and subsequent band bending, which results in an electric field near the surface. Kuball *et al.* explained deviations from the $\Delta E \propto N^{1/2}$ dependence in GaAs as the result of a carrier-depleted surface layer, which enhances the E_1 CP redshift.[64] For our GaN films studied here, the observed dependence of the E_1 CP energy on N may be influenced in a similar manner by impurity screening in bulk material and carrier-depleted surface layer effects. Quantitative analysis shall be the subject of further studies on well-defined surfaces of cubic GaN.

In contrast to the E_1 transition, the E_2 CP energy of GaN shows no significant dependence on the free-carrier concentration. For all three GaN samples R_1–R_3, the E_2 transition was observed at $\sim$7.55–7.58 eV, which is in excellent agreement with the E_2 CP energy value found by Logothetidis *et al.* for β-GaN at RT (7.58 ± 0.06 eV).[18] For α-GaN, the E_2 interband transition is reported to be in the range between 7.8 and 8.0 eV,[61–63] i.e., significantly higher in energy than for cubic material. Since the E_2 CP structure in β-GaN is not attributed to a single interband transition but composed of several CP's in different regions of the Brillouin zone, a detailed analysis of this structure is quite difficult. Nevertheless, the considerable increase of the broadening value of the E_2 CP feature with increasing N_e observed for our GaN films may indicate that the separation between the transitions contributing to the E_2 CP feature varies with N_e. For GaAs, several authors reported the dependence of the E_2 CP on doping and thus on the free-carrier concentration with ambiguous results. While Cardona *et al.*[66] found the E_2 CP energy in GaAs to be independent of the free-carrier concentration, Lukeš *et al.*[65] observed a power-law dependence of the E_2 CP energy.

Now we discuss the E_1 and E_2 CP behavior in $Al_xGa_{1-x}N$. For hexagonal $Al_xGa_{1-x}N$, Wethkamp *et al.*[61,67] determined the composition dependence of the E_1 and E_2 CP's in the entire composition range using SE and found an approximately linear increase of both transition energies with increasing Al content. Likewise, Cobet *et al.*[63] observed the E_1 and E_2 CP's in α-$Al_{0.1}Ga_{0.9}N$ shifting towards higher energies by 0.11 and 0.09 eV, respectively, compared to α-GaN. Furthermore, Benedict *et al.*[62] calculated $\varepsilon(\omega)$ of the end components α-GaN and α-AlN within a first-principles electronic structure scheme and found a blueshift of $\approx$0.7 eV for both the E_1 and E_2 interband transitions of α-AlN relative to those of α-GaN, which agrees well with SE measurements reported by the same authors. According to these results for hexagonal materials, with increasing Al content and at constant free-electron concentration one should expect the E_1 and E_2 interband transitions of cubic $Al_xGa_{1-x}N$ shifting towards those of β-AlN, which, however, are still unknown but are presumed not to differ much from those observed for α-AlN at $\approx$7.8 and 8.8 eV, respectively.[67]

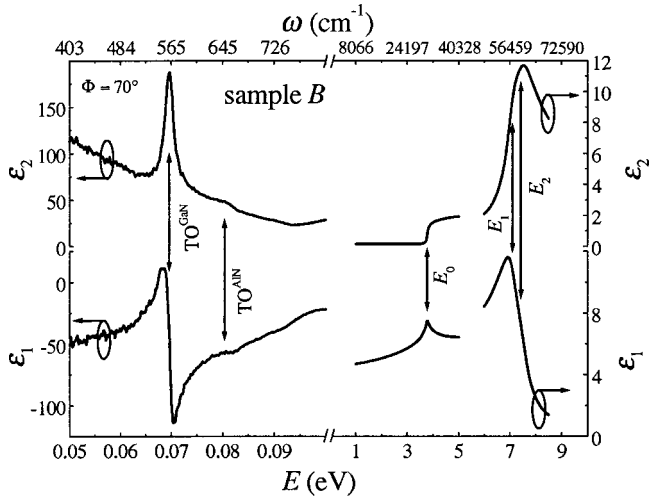

FIG. 11. Complex dielectric function of the $Al_{0.12}Ga_{0.88}N$ film (sample *B*), determined by the SE data analyses from the mid-ir to the vuv spectral range.

Provided that the free-carrier-induced E_1 CP shifting mechanisms for $Al_xGa_{1-x}N$ are similar to those observed for GaN, the alloy-induced shift of the E_1 CP is superimposed by the free-carrier-induced shift, and hence, only a qualitative discussion of the results obtained for our $Al_xGa_{1-x}N$ films is possible here. In fact, the E_1 transition of our $Al_{0.07}Ga_{0.93}N$ film (sample *A*) with $N_e \approx 7 \times 10^{19}\text{cm}^{-3}$ is blueshifted by $\sim$0.13 eV compared to the GaN film R_3 ($N_e = 5.1 \times 10^{19}$ cm^{-3}). Considering that $Al_{0.12}Ga_{0.88}N$ (sample *B*) possesses a larger free-carrier concentration and thus a stronger free-carrier-induced E_1 CP shift than the $Al_{0.07}Ga_{0.93}N$ film (sample *A*), the alloy-induced E_1 CP blueshift for the sample *B* is significantly larger than that for sample *A*. Thus, we can constitute that for $x \leqslant 0.12$ the alloy-induced blueshift of the E_1 CP energy increases with increasing Al content, as is expected.

In contradiction to the expected monotonic blueshift of the E_2 transition with increasing Al content, the E_2 CP's of the $Al_{0.07}Ga_{0.93}N$ and $Al_{0.12}Ga_{0.88}N$ films are found more than 0.10 eV below that of GaN. Again, since the spectral feature attributed here to the E_2 CP is composed of several interband transitions with similar transition energies, a detailed analysis of the E_2 spectral region is difficult. The observed behavior of the E_2 CP feature for our $Al_xGa_{1-x}N$ films is unexpected but not unusual. Studying $Al_xGa_{1-x}As$ with SE in the entire composition range, Logothetidis *et al.*[68] observed redshifts of the E_2 CP features with increasing Al content as well.

For $x \geqslant 0.16$, the interband transitions E_1 and E_2 cannot be differentiated anymore, and a single broad maximum occurs in the $\langle \varepsilon_2 \rangle$ spectra (Figs. 9 and 10), which is obviously blueshifted for $x=0.20$ (sample *D*) with respect to $x=0.16$ (sample *C*).

Finally, Fig. 11 depicts the complex dielectric function of $Al_{0.12}Ga_{0.88}N$ (sample *B*) exemplarily, which was obtained from the measured pseudodielectric function given in Fig. 1, performing SE data analyses from the mid-ir to the vuv spectral range.

V. SUMMARY

In summary, we studied the vibrational properties and the optical interband transitions E_0, E_1, and E_2 of cubic $Al_xGa_{1-x}N$ films ($0 \leqslant x \leqslant 0.20$) grown by radio-frequency plasma-assisted molecular-beam epitaxy. Spectroscopic ellipsometry from the mid-infrared to the vacuum-ultraviolet spectral range (0.05–8.5 eV) was employed for our investigations. Cubic $Al_xGa_{1-x}N$ for $x \leqslant 0.20$ shows a two-mode behavior for the TO-phonon, in agreement with recent theoretical predictions. The fundamental band-gap energy E_0 of the highly *n*-conductive $Al_xGa_{1-x}N$ films depends approximately linearly on the Al content with E_0 (eV) $= 3.19 + 2.77x$ upon consideration of the strong Burstein-Moss shift and band-gap renormalization effects. This composition dependence of the band-gap energy agrees excellently with recent theoretical predictions. The interband transition E_1 of cubic GaN becomes redshifted with increasing free-electron concentration, whereas the energetic position of the interband transition E_2 of GaN is found to be independent of the free-electron concentration. For $x \leqslant 0.12$, the E_1 (E_2) transition of $Al_xGa_{1-x}N$ shifts to higher (lower) energies with increasing Al content.

ACKNOWLEDGMENTS

This work was supported by DFG under Grants Nos. Rh 28-3/2 and As 107/1-3 and by NSF Contract No. DMI-9901510. The authors thank Professor M. Grundmann, Professor W. Grill, and Professor B. Rheinländer for continuing interest.

*Electronic address: pge95ipi@studserv.uni-leipzig.de; URL: http://www.uni-leipzig.de/~hlp/ellipsometrie

[1] J. Wu, H. Yaguchi, K. Onabe, and Y. Shiraki, J. Cryst. Growth **197**, 73 (1999).

[2] A. Nakadaira and H. Tanaka, J. Cryst. Growth **189/190**, 411 (1998).

[3] T. Frey, D.J. As, M. Bartels, A. Pawlis, K. Lischka, A. Tabata, J.R.L. Fernandez, M.T.O. Silva, J.R. Leite, C. Haug, and R. Brenn, J. Appl. Phys. **89**, 2631 (2001).

[4] D.J. As, T. Frey, M. Bartels, K. Lischka, R. Goldhahn, S. Shokhovets, A. Tabata, J.R.L. Fernandez, and J.R. Leite, J. Cryst. Growth **230**, 421 (2001).

[5] D.J. As, T. Frey, M. Bartels, A. Khartchenko, D. Schikora, K. Lischka, R. Goldhahn, and S. Shokhovets, in *GaN and Related Alloys*, edited by U. Mishra, M.S. Shur, C.M. Wetzel, B. Gil, and K. Kishino, MRS Symposia Proceedings No. 639, (Materials Research Society, Pittsburgh, 2001), p. G5.9.

[6] H. Okumura, H. Hamaguchi, T. Koizumi, K. Balakrishnan, Y. Ishida, M. Arita, S. Chichibu, H. Nakanishi, T. Nagatomo, and S. Yoshida, J. Cryst. Growth **189/190**, 390 (1998).

[7] T. Koizumi, H. Okumura, K. Balakrishnan, H. Harima, T. Inoue, Y. Ishida, T. Nagatomo, S. Nakashima, and S. Yoshida, J. Cryst. Growth **201/202**, 341 (1999).

[8] H. Okumura, T. Koizumi, Y. Ishida, H. Yaguchi, and S. Yoshida, Phys. Status Solidi B **216**, 211 (1999).

[9] T. Suzuki, H. Yaguchi, H. Okumura, Y. Ishida, and S. Yoshida, Jpn. J. Appl. Phys., Part 2 **39**, L497 (2000).

[10] D.P. Xu, H. Yang, D.G. Zhao, J.B. Li, L.X. Zheng, Y.T. Wang, S.F. Li, L.H. Duan, and R.H. Wu, J. Cryst. Growth **203**, 40 (1999).

[11] J. Wu, H. Yaguchi, K. Onabe, and Y. Shiraki, Appl. Phys. Lett. **73**, 193 (1998).

[12] A. Nakadaira and H. Tanaka, Appl. Phys. Lett. **70**, 2720 (1997).

[13] A. Nakadaira and H. Tanaka, Jpn. J. Appl. Phys., Part 1 **37**, 1449 (1998).

[14] H. Grille, C. Schnittler, and F. Bechstedt, Phys. Rev. B **61**, 6091 (2000).

[15] M.S. Liu, L.A. Bursill, and S. Prawer, Mod. Phys. Lett. B **12**, 443 (1998).

[16] H. Harima, T. Inoue, S. Nakashima, H. Okumura, Y. Ishida, S. Yoshida, T. Koizumi, H. Grille, and F. Bechstedt, Appl. Phys. Lett. **74**, 191 (1999).

[17] S.K. Pugh, D.J. Dugdale, S. Brand, and R.A. Abram, J. Appl. Phys. **86**, 3768 (1999).

[18] S. Logothetidis, J. Petalas, M. Cardona, and T.D. Moustakas, Phys. Rev. B **50**, 18 017 (1994).

[19] P.Y. Yu and M. Cardona, *Fundamentals of Semiconductors* (Springer, Berlin, 1996).

[20] A. Kasic, M. Schubert, S. Einfeldt, D. Hommel, and T.E. Tiwald, Phys. Rev. B **62**, 7365 (2000).

[21] A. Kasic, M. Schubert, J. Off, and F. Scholz, Appl. Phys. Lett. **78**, 1526 (2001).

[22] M. Schubert, A. Kasic, S. Einfeldt, D. Hommel, U. Köhler, D.J. As, J. Off, B. Kuhn, F. Scholz, and J.A. Woollam, Phys. Status Solidi B **228**, 437 (2001).

[23] T. Hofmann, G. Leibiger, V. Gottschalch, I. Pietzonka, and M. Schubert, Phys. Rev. B **64**, 155206 (2001).

[24] J. Humlíček, R. Henn, and M. Cardona, Appl. Phys. Lett. **69**, 2581 (1996).

[25] J. Wagner, H. Obloh, M. Kunzer, M. Maier, K. Köhler, and B. Johs, J. Appl. Phys. **89**, 2779 (2001), and references therein.

[26] G. Leibiger, V. Gottschalch, B. Rheinländer, J. Šik, and M. Schubert, J. Appl. Phys. **89**, 4927 (2001).

[27] G. Leibiger, V. Gottschalch, and M. Schubert, J. Appl. Phys. **90**, 5951 (2001).

[28] D. Schikora, M. Hankeln, D.J. As, K. Lischka, T. Litz, A. Waag, T. Buhrow, and F. Henneberger, Phys. Rev. B **54**, R8381 (1996).

[29] T.E. Tiwald, D.W. Thompson, and J.A. Woollam, J. Vac. Sci. Technol. B **16**, 312 (1998).

[30] R.M.A. Azzam and N.M. Bashara, *Ellipsometry and Polarized Light* (North-Holland, Amsterdam, 1984).

[31] C.M. Herzinger, H. Yao, P.G. Snyder, F.G. Celii, Y.-C. Kao, B. Johs, and J.A. Woollam, J. Appl. Phys. **77**, 4677 (1995).
[32] G.E. Jellison, Thin Solid Films **313-314**, 33 (1998).
[33] F. Gervais and B. Piriou, J. Phys. C **7**, 2374 (1974).
[34] C.M. Wolfe, N. Holonyak, and G.E. Stillmann, *Physical Properties of Semiconductors* (Prentice-Hall, Englewood Cliffs, NJ, 1989).
[35] D.W. Berreman, Phys. Rev. **130**, 2193 (1963).
[36] A. Röseler, *Infrared Spectroscopic Ellipsometry* (Akademie-Verlag, Berlin, 1990).
[37] J. Humlíček, Phys. Status Solidi B **215**, 155 (1999).
[38] M. Cardona, *Modulation Spectroscopy* (Academic, New York, 1969).
[39] D.E. Aspnes, in *Handbook on Semiconductors*, edited by T.S. Moss (North-Holland Amsterdam, 1980), Vol. II, pp. 109–154.
[40] J.W. Garland, H. Abad, M. Viccaro, and P.M. Raccah [Appl. Phys. Lett. **52**, 1176 (1988)] showed that the proper functional representation for the optical dielectric function of the zinc-blende semiconductors GaAs and CdTe has partial Gaussian contribution. They further demonstrated that varying the exponent μ_j in the Lorentzian representation of Eq. (7) effectively mimics the partial Gaussian broadening of the CP structure. In order to consider a possible partial Gaussian broadening of the CP features of our $Al_xGa_{1-x}N$ dielectric functions, the exponents μ_j for all three CP's E_0, E_1, and E_2 were allowed to vary during the data regression analysis.
[41] M. Ramsteiner, O. Brandt, and K.H. Ploog, Phys. Rev. B **58**, 1118 (1998).
[42] M. Giehler and E. Jahne, Phys. Status Solidi B **73**, 503 (1976).
[43] A one-mode behavior for the LO phonon of β-$Al_xGa_{1-x}N$ was theoretically predicted in Ref. 14.
[44] M. Fanciulli, T. Lei, and T.D. Moustakas, Phys. Rev. B **48**, 15 144 (1993).
[45] L.E. Ramos, L.K. Teles, L.M.R. Scolfaro, J.L.P. Castineira, A.L. Rosa, and J.R. Leite, Phys. Rev. B **63**, 165210 (2001).
[46] A. Kasic, M. Schubert, B. Kuhn, F. Scholz, S. Einfeldt, and D. Hommel, J. Appl. Phys. **89**, 3720 (2001).
[47] J. Petalas, S. Logothetidis, S. Boultadakis, M. Alouani, and J.M. Wills, Phys. Rev. B **52**, 8082 (1995).
[48] U. Köhler, D.J. As, B. Schöttker, T. Frey, K. Lischka, J. Scheiner, S. Shokhovets, and R. Goldhahn, J. Appl. Phys. **85**, 404 (1999).
[49] H. Teisseyre, P. Perlin, T. Suski, I. Grzegory, S. Porowski, J. Jun, A. Pietraszko, and T.D. Moustakas, J. Appl. Phys. **76**, 2429 (1994).
[50] D.C. Reynolds, D.C. Look, and B. Jogai, J. Appl. Phys. **88**, 5760 (2000).
[51] J.-L. Reverchon, F. Huet, M.-A. Poisson, and J.-Y. Duboz, J. Appl. Phys. **88**, 5138 (2000).
[52] P. K. Basu, *Theory of Optical Processes in Semiconductors* (Oxford University Press, Oxford, 1997).
[53] H.C. Casey, Jr. and F. Stern, J. Appl. Phys. **47**, 631 (1976).
[54] D.J. As, A. Richter, J. Busch, B. Schöttker, M. Lübbers, J. Mimkes, D. Schikora, K. Lischka, W. Kriegseis, W. Burkhardt, and B.K. Meyer, MRS Internet J. Nitride Semicond. Res. **5S1**, W3.81 (2000).
[55] M. Yoshikawa, M. Kunzer, J. Wagner, H. Obloh, P. Schlotter, R. Schmidt, N. Herres, and U. Kaufmann, J. Appl. Phys. **86**, 4400 (1999).
[56] In Refs. 8 and 9, the $Al_xGa_{1-x}N$ dielectric function near the fundamental band-gap was parametrized using Adachi's composite model formalism, S. Adachi, Phys. Rev. B **35**, 7454 (1987); **38**, 12 345 (1988).
[57] S.R. Lee, A.F. Wright, M.H. Crawford, G.A. Petersen, J. Han, and R.M. Biefeld, Appl. Phys. Lett. **74**, 3344 (1999).
[58] Such surface overlayers mostly reduce the absolute values of $\langle \varepsilon_2 \rangle$ compared to the bulk dielectric function ε_2. However, derivative spectra (see Fig. 10), which are most sensitive to the CP transition energy and broadening values, are not or only little affected by thin surface overlayers. To allow for surface-roughness effects, a linear effective-medium approximation was used as described in Sec. III.
[59] L.X. Benedict and E.L. Shirley, Phys. Rev. B **59**, 5441 (1999).
[60] C. Janowitz, M. Cardona, R. L. Johnson, T. Cheng, T. Foxon, O. Gunther, and G. Jungk, Jahresbericht BESSY No. 230, 1994 (unpublished).
[61] T. Wethkamp, K. Wilmers, N. Esser, W. Richter, O. Ambacher, H. Angerer, G. Jungk, R.L. Johnson, and M. Cardona, Thin Solid Films **313-314**, 745 (1998).
[62] L.X. Benedict, T. Wethkamp, K. Wilmers, C. Cobet, N. Esser, E.L. Shirley, W. Richter, and M. Cardona, Solid State Commun. **112**, 129 (1999).
[63] C. Cobet, N. Esser, J.T. Zettler, W. Richter, P. Waltereit, O. Brandt, K.H. Ploog, S. Peters, N.V. Edwards, O.P.A. Lindquist, and M. Cardona, Phys. Rev. B **64**, 165203 (2001).
[64] M. Kuball, M.K. Kelly, M. Cardona, K. Köhler, and J. Wagner, Phys. Rev. B **49**, 16 569 (1994).
[65] F. Lukeš, S. Gopalan, and M. Cardona, Phys. Rev. B **47**, 7071 (1993).
[66] M. Cardona, K.L. Shaklee, and F.H. Pollak, Phys. Rev. **154**, 696 (1967).
[67] T. Wethkamp, K. Wilmers, C. Cobet, N. Esser, W. Richter, O. Ambacher, M. Stutzmann, and M. Cardona, Phys. Rev. B **59**, 1845 (1999).
[68] S. Logothetidis, M. Alouani, M. Garriga, and M. Cardona, Phys. Rev. B **41**, 2959 (1990).